



Mathematical Model of Tumour Spheroid Experiments with Real-Time Cell Cycle Imaging

Wang Jin¹ · Loredana Spoerri² · Nikolas K. Haass² · Matthew J. Simpson¹ 

Received: 7 December 2020 / Accepted: 26 February 2021 / Published online: 20 March 2021
© The Author(s), under exclusive licence to Society for Mathematical Biology 2021

Abstract

Three-dimensional (3D) *in vitro* tumour spheroid experiments are an important tool for studying cancer progression and potential cancer drug therapies. Standard experiments involve growing and imaging spheroids to explore how different conditions lead to different rates of spheroid growth. These kinds of experiments, however, do not reveal any information about the spatial distribution of the cell cycle within the expanding spheroid. Since 2008, a new experimental technology called fluorescent ubiquitination-based cell cycle indicator (FUCCI) has enabled real-time *in situ* visualisation of the cell cycle progression. Observations of 3D tumour spheroids with FUCCI labelling reveal significant intratumoural structure, as the cell cycle status can vary with location. Although many mathematical models of tumour spheroid growth have been developed, none of the existing mathematical models are designed to interpret experimental observations with FUCCI labelling. In this work, we adapt the mathematical framework originally proposed by Ward and King (Math Med Biol 14:39–69, 1997. <https://doi.org/10.1093/imammb/14.1.39>) to produce a new mathematical model of FUCCI-labelled tumour spheroid growth. The mathematical model treats the spheroid as being composed of three subpopulations: (i) living cells in G1 phase that fluoresce red; (ii) living cells in S/G2/M phase that fluoresce green; and (iii) dead cells that are not fluorescent. We assume that the rates at which cells pass through different phases of the cell cycle, and the rate of cell death, depend upon the local oxygen concentration. Parameterising the new mathematical model using experimental measurements of cell cycle transition times, we show that the model can qualitatively capture important experimental observations that cannot be addressed using previous

Nikolas K. Haass and Matthew J. Simpson have contributed equally.

✉ Matthew J. Simpson
matthew.simpson@qut.edu.au

¹ School of Mathematical Sciences, Queensland University of Technology (QUT), Brisbane, Australia

² The University of Queensland Diamantina Institute, Translational Research Institute, The University of Queensland, Brisbane, Australia

mathematical models. Further, we show that the mathematical model can be used to qualitatively mimic the action of anti-mitotic drugs applied to the spheroid. All software programs required to solve the nonlinear moving boundary problem associated with the new mathematical model are available on GitHub, at <https://github.com/wang-jin-mathbio/Jin2021>

Keywords Mathematical modelling · Tumour spheroid · Cell cycle · Cancer · Moving boundary problem

1 Introduction

In vitro three-dimensional (3D) tumour spheroids have been widely used to study cancer progression and putative therapies (Kunz-Schughart et al. 1998; Nath and Devi 2016; Santini and Rainaldi 1999; Spoerri et al. 2017). The generation and analysis of tumour spheroids have been documented in the literature for approximately fifty years (Sutherland et al. 1971; Greenspan 1972). Traditional spheroid experiments involve growing populations of cancer cells in 3D culture, and visualising spheroid growth and invasion by taking phase contrast images (Beaumont et al. 2014). As an illustrative example, the image in Fig. 1a shows a spheroid generated from C8161 melanoma cells. In some experiments, the formation of a necrotic core within the spheroid can be examined using fluorescent live/dead assays (e.g. Calcein-AM/Ethidium bromide or DRAQ7) and used to assess drug cytotoxicity (Chan et al. 2003; Maeda et al. 2014; Smalley et al. 2008; Kienzle et al. 2017). This standard experimental protocol provides very little insight into cell cycle behaviour and spatio-temporal distribution patterns of proliferating cells, within the growing spheroid.

Spheroids mimic physiological tumour features, such as cell cycle behaviour, which is responsible for tumour cell proliferation and thus tumour growth, but also invasion, cell–cell and cell–matrix interactions, molecule diffusion, oxygen/nutrient gradients (with a hypoxic zone and a central necrosis) as well as drug sensitivity (Beaumont

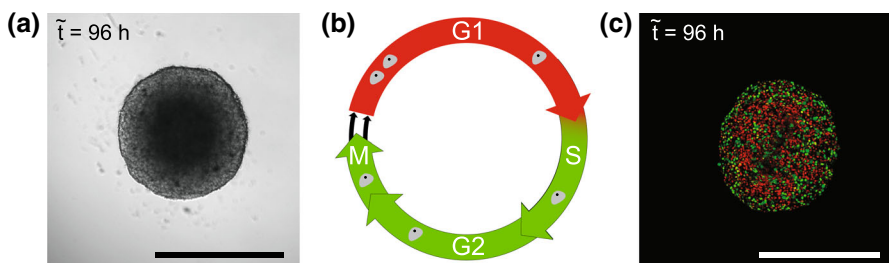


Fig. 1 (Colour Figure Online) Motivating images and cell cycle schematic. **a** Phase contrast image of a 3D melanoma spheroid with the C8161 cell line grown on agar after 96 h. The scale bar corresponds to 600 μm . **b** Schematic of the eukaryotic cell cycle indicating the transition between different phases together with the red and green fluorescence colours associated with fluorescent ubiquitination-based cell cycle indicator (FUCCI) labelling. For the purpose of this study, we neglect double positivity (yellow) in early S phase. **c** Confocal microscopy image of a 3D melanoma spheroid after 96 h, using FUCCI-transduced C8161 melanoma cells. The scale bar corresponds to 600 μm

et al. 2014; Smalley et al. 2008; Spoerri et al. 2017). The cell cycle consists of a sequence of four distinct phases: gap 1 (G1), synthesis (S), gap 2 (G2), and the mitotic (M) phase, as illustrated in Fig. 1b. The G1, S, and G2 phases are collectively referred to as *interphase*, which involves cell growth and preparation for division. After interphase, the cell enters the mitotic phase and divides into two daughter cells. Since 2008 (Sakaue-Sawano et al. 2008), a new experimental technique called *fluorescent ubiquitination-based cell cycle indicator* (FUCCI) has enabled real-time *in situ* visualisation of the cell cycle progression from G1 to S/G2/M in individual cells. The FUCCI system consists of two fluorescent probes which emit red fluorescence when the cell is in the G1 phase, or green fluorescence when the cell is in S/G2/M phase (Sakaue-Sawano et al. 2008), as shown schematically in Fig. 1b. Before the development of FUCCI, it was difficult to examine the cell cycle dynamics of individual cells within a growing population. The spheroids in Fig. 1 are constructed with the same melanoma cell line: C8161 (Fig. 1a) and C8161 expressing FUCCI (Fig. 1c). The key difference is that FUCCI reveals more detailed information about the cell cycle status at different locations within the growing spheroid. In Fig. 1c, we see that the spheroid periphery has an even distribution of red and green cells, indicating that they are in active cell cycle, i.e. proliferating. In contrast, cells in the spheroid centre are predominantly red, indicating G1-arrest (Haass et al. 2014). This information, revealed by FUCCI, allows us to visualise and measure both the time evolution of the spheroid size and spatial patterns of cell cycle behaviour within the spheroid (Haass et al. 2014). Understanding the biology of cell cycle behaviour is important, as cell cycle phase-specific drug resistance has been described as an escape mechanism of cancer cells (Beaumont et al. 2016; Haass and Gabrielli 2017).

Several mathematical models have been developed to describe experimental tumour spheroids. The development of these mathematical models began in the 1970s (Greenspan 1972; McElwain and Morris 1978; McElwain et al. 1979; Norton et al. 1976). The seminal mathematical model by Greenspan (1972) idealises a tumour spheroid as a compound sphere: the inner-most region is a necrotic core containing dead cells; the intermediate spherical shell contains living, non-proliferative, or *quiescent* cells; and the outer-most spherical shell contains live, freely proliferating cells. A key assumption in Greenspan's model is that cell proliferation is limited by the availability of a nutrient, such as oxygen. Greenspan (1972) assumes that oxygen diffuses into the spheroid from the free, growing surface. Living cells are assumed to consume oxygen, and those cells die when there is insufficient oxygen available locally. A further assumption is that dead cells produce a chemical inhibitor, such as metabolites, that diffuse from the necrotic core towards the growing surface of the spheroid. Assembling these assumptions together in terms of a spherically symmetric conservation statement, Greenspan's model can be written as a system of coupled partial differential equations (PDE). The solution of these PDEs describes the time evolution of the spheroid in terms of: (i) the radius of the necrotic core; (ii) the thickness of the spherical shell containing quiescent cells; and, (iii) the outer radius of the spheroid (Greenspan 1972).

Since Greenspan's model was first proposed, a number of partially refined models have been introduced (e.g. Deakin 1975; Pettet et al. 2001; Ward and King 1997; Flegg and Nataraj 2019; Sarapata and de Pillis 2014). An important contribution is

the work of Ward and King (1997) who proposed a mathematical model describing a spherically symmetric population of cells that is composed of a subpopulation of live cells and a subpopulation of dead cells. This model also considers the spatial and temporal distribution of some nutrient, which is again taken to be oxygen. Ward and King (1997) assume that living cells proliferate with a rate that depends on the local oxygen concentration, and that the act of proliferation consumes oxygen. Further, living cells are assumed to die, and death rate is also a function of local oxygen concentration. All cells in the spheroid move with a local velocity field that is created by net volume gain as a result of cell proliferation and cell death, since they make the reasonable assumption that the volume of a dead cell is less than the volume of a living cell. Together, these assumptions lead to a novel moving boundary PDE model. The solution of this moving boundary problem can, for certain choices of parameters, lead to the formation of a necrotic core in the growing spheroid (Ward and King 1997). A key difference between the models of Greenspan (1972) and Ward and King (1997) is that the former defines the interfaces between the necrotic core and the quiescent zone, and between the quiescent zone and the freely proliferating zone to be perfectly sharp well-defined interfaces, while the latter is continuous, and the internal boundaries are less well defined. Other approaches to modelling tumour spheroids, including multiphase models, have also been developed (Breward et al. 2002; Byrne et al. 2003; Chaplain et al. 2006; Collis et al. 2016; Enderling and Chaplain 2014; Landman and Please 2001; Lewin et al. 2020; Spill et al. 2016), but these models do not explicitly include cell cycle labelling. The primary aim of this work is to reformulate the model by Ward and King (1997) so that their framework can be used to describe spheroid experiments with FUCCI labelling. While, in principal, any of the more recent tumour spheroid models could also be reformulated to incorporate FUCCI labelling, here we focus on the work of Ward and King (1997) because their model is widely adopted.

In this study, we present a mathematical model of *in vitro* tumour spheroids that is an extension of Ward and King's modelling framework. The key feature of our model is that we explicitly incorporate the transition between different phases of the cell cycle so that the model can be applied to tumour spheroids with FUCCI labelling. Our model considers the spheroid to be composed of three subpopulations: (i) living cells in G1 phase that fluoresce red; (ii) living cells in S/G2/M phase that fluoresce green; and (iii) non-fluorescent dead cells. We assume that the rates at which cells progress through the cell cycle depend upon the local oxygen concentration, and that the rate of cell death also depends on the local oxygen concentration in the spheroid. We partially parameterise the new mathematical model using existing experimental measurements of cell cycle transition times, and then, using additional carefully chosen parameter values, we show that the model captures important experimental observations that cannot be observed in standard experiments without FUCCI labelling. We conclude by qualitatively exploring how the model can be used to simulate the application of anti-mitotic drugs.

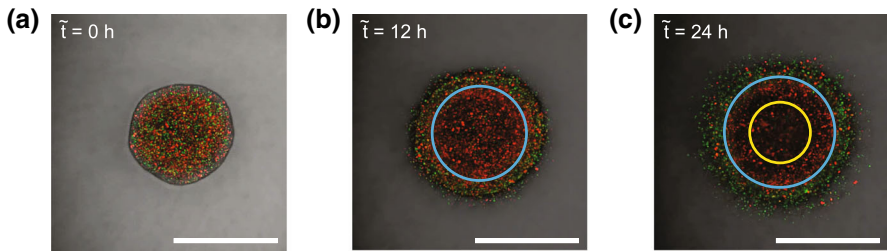


Fig. 2 (Colour Figure Online) In vitro tumour spheroid generated with FUCCI-C8161 melanoma cells. **a–c** The University of Queensland Diamantina Institute, Translational Research Institute Still images from a time lapse movie over 24 h, with the times as indicated. **a** The red and green fluorescing cells relatively evenly distributed throughout the spheroid. **b** A mixture of red and green fluorescing cells at the surface of the spheroid, whereas in the centre of the spheroid we see predominantly red fluorescing cells. **c** The inner-most region is largely free of fluorescing cells; the intermediate region contains mostly red fluorescing cells; and the outermost region contains a mixture of red and green fluorescing cells. Blue and yellow concentric circles are superimposed on **b**, **c** to show the approximate boundaries between these zones. The scale bars correspond to 500 μm

2 Experimental Motivation

Our modelling work is motivated by experimental observations of tumour spheroids with FUCCI labelling, such as the image in Fig. 1c. In Fig. 2, we present snapshots from a time-lapse movie of FUCCI-labelled spheroid growth, again with FUCCI-C8161 melanoma cells. At early time, $\tilde{t} = 0$ h, we see that the spheroid is relatively homogeneous and composed of well-mixed red and green fluorescing cells with no obvious spatial patterns. At intermediate time, $\tilde{t} = 12$ h, the spheroid has expanded in radius, and the central region of the spheroid is composed mostly of cells in G1 phase (red), whereas the outer shell of the spheroid contains well-mixed red and green fluorescing cells. At later time, $\tilde{t} = 24$ h, we see the spheroid continues to expand in size. In this case, the outer spherical shell contains well-mixed red and green fluorescing cells, an intermediate spherical shell is composed of predominantly red fluorescing cells, whereas the absence of fluorescence in the central region indicates the formation of a necrotic core. These images show the importance of FUCCI labelling as this information indicates that we have a strong correlation between the spatial position and the cell cycle status. In a spheroid without FUCCI labelling, such as in the image in Fig. 1a, it is not possible to see this level of detail. Further, this tight coupling between location and cell cycle status illustrates the biological importance of working in a 3D geometry, as it is largely absent in two-dimensional (2D) experiments where all cells in the population have access to oxygen since these experiments involve a thin monolayer of cells (Haass et al. 2014; Vittadello et al. 2018, 2019, 2020; Simpson et al. 2018, 2020).

We hypothesise that the simplest explanation of the spatial patterns in cell cycle status in Fig. 2 is caused by differences in local nutrient availability. As in the case of Greenspan (1972) and Ward and King (1997), we make the assumption that the key nutrient of interest is oxygen. Furthermore, if we assume that oxygen diffuses into the spheroid from the free surface, we expect that cells near the spheroid surface

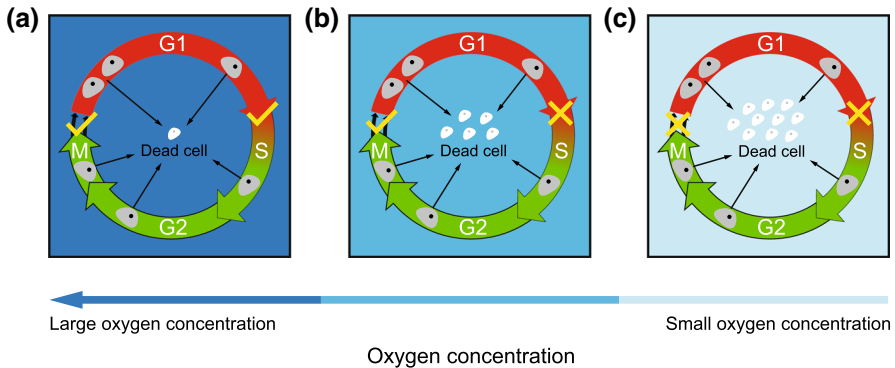


Fig. 3 (Colour Figure Online) Schematic of oxygen-dependent transitions in the cell cycle with FUCCI labelling. **a** When oxygen is abundant, cells in G1 phase (red) transition to S/G2/M phase (green), and cells in S/G2/M phase (green) divide into two daughter cells in G1 phase (red). **b** When oxygen availability is reduced, cells in S/G2/M phase (green) continue through the cell cycle and divide into two daughter cells in G1 phase (red); however, those cells in G1 phase (red) do not have access to sufficient oxygen to proceed through the cell cycle. **c** When oxygen availability is sufficiently reduced, both G1-arrest (i.e. interruption of the transition from red to green) and G2-arrest (i.e. interruption of the transition from green to red) are induced

will have access to sufficient oxygen to proliferate freely. Since cells consume oxygen to survive and proliferate, we anticipate that the oxygen concentration will decrease with depth from the spheroid surface. Accordingly, at some depth, we expect that there could be sufficient oxygen to enable cell survival, but insufficient to allow cells to enter the cell cycle. This would explain the formation of a living, quiescent, G1-arrested population of cells at intermediate depths within the sphere. At locations deeper within the spheroid still, where oxygen concentration would be smallest, the local oxygen concentration would be insufficient to support living cells, giving rise to a necrotic region.

To translate these biological observations and assumptions into a mathematical model, we first present a schematic of the cell cycle, coupled with FUCCI labelling, in Fig. 3. The schematic in Fig. 3a, for plentiful oxygen availability, indicates that the cell cycle proceeds freely, and cells in G1 phase (red) enter the cell cycle at a particular rate and proceed through the S/G2/M phase (green) before dividing, at another particular rate, into two daughter cells in G1 phase (red). In this schematic, we also allow all living cells to undergo some intrinsic death process. The schematic in Fig. 3b, for intermediate oxygen availability, indicates that the cell cycle is interrupted by the reduced oxygen availability. Under these intermediate oxygen conditions, cells in G1 phase (red) are not able to enter the cell cycle because of the reduced oxygen availability. Those cells already in S/G2/M phase (green) are able to continue through the cell cycle before dividing, to produce two daughter cells in G1 phase (red). The schematic in Fig. 3c, for further reduced oxygen availability, indicates that both G1-arrest (i.e. interruption of the transition from red to green) and G2-arrest (i.e. interruption of the transition from green to red) could be induced through the reduced oxygen availability. In this case, we expect that the dominant mechanism affecting the population dynamics is localised cell death.

Based on the experimental observations in Fig. 2 (Haass et al. 2014), and the schematic in Fig. 3, we now construct a mathematical model that can be used to interpret experimental data describing 3D tumour spheroids with FUCCI by extending the framework originally proposed by Ward and King (1997).

3 Model Formulation

In the initial presentation of the model, we consider all quantities to be dimensional and denote using a tilde. Later, we will simplify the model by nondimensionalising all dependent and independent variables. All nondimensional quantities are denoted using regular variables, without the tilde. We take \tilde{r} to be the volume fraction of red fluorescing cells (G1 phase) and \tilde{g} to be the volume green fluorescing cells (S/G2/M phase), so that $\tilde{n} = \tilde{r} + \tilde{g}$ is the volume fraction of living cells, and we suppose that \tilde{m} is the volume fraction of dead cells. Mass conservation of the \tilde{r} and \tilde{g} subpopulations is governed by the transitions between different phases of the cell cycle, cell death, and transport by a local velocity field, \tilde{v} , giving

$$\frac{\partial \tilde{r}}{\partial t} + \underbrace{\nabla \cdot (\tilde{v}\tilde{r})}_{\text{advective transport}} = \underbrace{2\tilde{K}_g(\tilde{c})\tilde{g} - \tilde{K}_r(\tilde{c})\tilde{r}}_{\text{FUCCI-labelled cell cycle}} - \underbrace{\tilde{K}_d(\tilde{c})\tilde{r}}_{\text{cell death}}, \tag{1}$$

$$\frac{\partial \tilde{g}}{\partial t} + \underbrace{\nabla \cdot (\tilde{v}\tilde{g})}_{\text{advective transport}} = \underbrace{\tilde{K}_r(\tilde{c})\tilde{r} - \tilde{K}_g(\tilde{c})\tilde{g}}_{\text{FUCCI-labelled cell cycle}} - \underbrace{\tilde{K}_d(\tilde{c})\tilde{g}}_{\text{cell death}}, \tag{2}$$

where $\tilde{K}_r(\tilde{c}) > 0$ is the rate of transition from G1 to S/G2/M phase, $\tilde{K}_g(\tilde{c}) > 0$ is the rate of transition from S/G2/M to G1 phase, and $\tilde{K}_d(\tilde{c}) > 0$ is the rate of cell death. The key feature of our model is that each of these rates depends upon the local oxygen concentration, $\tilde{c} > 0$. The source terms in (1)–(2) have a relatively simple interpretation. The negative source terms in Eq. (1) represent the local loss of cells in G1 phase owing to cell death and the progression through the cell cycle. The positive source term in Eq. (2) represents the increase in cells in G2 phase as a result of cells in G1 phase progressing through the cell cycle. The negative source terms in Eq. (2) represent the local decrease cells in G2 phase owing to cell death and the progression through the cell cycle. The positive source term in Eq. (1) represents the local increase in cells in G1 phase due to the cell cycle, and the factor of two represents the fact that each cell passing from S/G2/M phase to G1 phase produces two daughter cells in G1 phase (Vittadello et al. 2018; Simpson et al. 2020). A notable feature of this nutrient-dependent cell proliferation and cell death framework is that it avoids the need for specifying a carrying capacity density as a model parameter, such as in the ubiquitous logistic growth model (Maini et al. 2004a, b; Jin et al. 2016, 2017, 2019).

The spatial and temporal distribution of the fraction of dead cells can also be described in terms of a PDE,

$$\frac{\partial \tilde{m}}{\partial \tilde{t}} + \overbrace{\nabla \cdot (\tilde{v} \tilde{m})}^{\text{advective transport}} = \overbrace{\tilde{K}_d(\tilde{c})\tilde{r} + \tilde{K}_d(\tilde{c})\tilde{g}}^{\text{cell death}}. \tag{3}$$

Following Ward and King (1997), we assume the local velocity is associated with net volume gain associated with cell proliferation and cell death,

$$\nabla \cdot \tilde{v} = \overbrace{\tilde{K}_g(\tilde{c})\tilde{g}\tilde{V}_L}^{\text{increase in volume}} - \overbrace{\tilde{K}_d(\tilde{c})(\tilde{r} + \tilde{g})(\tilde{V}_L - \tilde{V}_D)}^{\text{decrease in volume}}, \tag{4}$$

where $\tilde{V}_L > 0$ and $\tilde{V}_D > 0$ are the volumes of single living and dead cells, respectively. The first term on the right of Eq. (4) represents the increase in volume by mitosis, whereas the second term on the right of Eq. (4) is the net decrease in volume by cell death. Here we assume that the volume of all living cells is the same, regardless of whether they are in G1 or S/G2/M phase.

Again following Ward and King (1997), we assume oxygen is transported through the continuum of live and dead cell mixture with the local velocity, \tilde{v} . We incorporate some oxygen diffusion, with diffusivity $\tilde{D} > 0$, and that oxygen is consumed by living cells, giving rise to

$$\frac{\partial \tilde{c}}{\partial \tilde{t}} + \overbrace{\nabla \cdot (\tilde{v} \tilde{c})}^{\text{advective transport}} = \overbrace{\nabla \cdot (\tilde{D} \nabla \tilde{c})}^{\text{diffusion}} - \underbrace{\tilde{\beta} \tilde{K}_g(\tilde{c})\tilde{g}}_{\text{mitosis}} - \underbrace{\tilde{\gamma}(\tilde{c})(\tilde{r} + \tilde{g})}_{\text{metabolism}}, \tag{5}$$

here $\tilde{\gamma}(\tilde{c}) > 0$ is the rate at which living cells consume oxygen through regular metabolic activity and $\tilde{\beta}(\tilde{c}) > 0$ is the rate at which oxygen is consumed during mitosis.

In this model, the kinetic rate functions $\tilde{K}_g(\tilde{c}) > 0$, $\tilde{K}_r(\tilde{c}) > 0$, and $\tilde{K}_d(\tilde{c}) > 0$ encode critical information about how the rate of transitions between subpopulation \tilde{r} , \tilde{g} , and \tilde{m} depends upon local oxygen concentration. Extending the approach of Ward and King (1997), we suppose these rate functions can be expressed in terms of Hill functions

$$\tilde{K}_g(\tilde{c}) = \frac{\tilde{A} \tilde{c}^{m_1}}{\tilde{c}_g^{m_1} + \tilde{c}^{m_1}}, \tag{6}$$

$$\tilde{K}_r(\tilde{c}) = \frac{\tilde{B} \tilde{c}^{m_2}}{\tilde{c}_r^{m_2} + \tilde{c}^{m_2}}, \tag{7}$$

$$\tilde{K}_d(\tilde{c}) = \tilde{C} \left(1 - \frac{\sigma \tilde{c}^{m_3}}{\tilde{c}_d^{m_3} + \tilde{c}^{m_3}} \right), \tag{8}$$

where $\tilde{A} > 0$ is the maximum rate at which cells transition from S/G2/M (green) phase to G1(red) phase; $\tilde{B} > 0$ is the maximum rate at which cell transition from G1 (red) phase to S/G2/M (green) phase; $\tilde{C} > 0$ is the maximum rate at which cells die; $m_1 > 0$, $m_2 > 0$, and $m_3 > 0$ are exponents in the Hill functions that govern the steepness about the critical oxygen concentrations $\tilde{c}_g > 0$, $\tilde{c}_r > 0$, and $\tilde{c}_d > 0$, respectively. To ensure $\tilde{K}_d > 0$, we require $0 \leq \sigma \leq 1$. Our choice of working with Hill functions in Eqs. (6)–(8) is not unique, and other functional forms could be used. Here we choose to work with Hill functions because this is consistent with the original model of Ward and King (1997).

Some further assumptions are required to completely specify the mathematical model. First, assuming there are no voids in the spheroids leads to

$$\tilde{V}_L \tilde{n} + \tilde{V}_D \tilde{m} = 1. \tag{9}$$

Second, we make the usual assumption that the spheroid is spherically symmetric so that the two independent variables are the radial position, \tilde{x} , and time, \tilde{t} . This gives $0 \leq \tilde{x} \leq \tilde{l}(\tilde{t})$, where $\tilde{l}(\tilde{t})$ is the radius of the spheroid at time \tilde{t} . To close the model, we specify initial conditions and boundary conditions. Initially, we assume that the spheroid is a mixture of living cells only, leading to

$$\tilde{r}(\tilde{x}, 0) = \frac{N_r}{(N_r + N_g) \tilde{V}_L}, \quad \tilde{g}(\tilde{x}, 0) = \frac{N_g}{(N_r + N_g) \tilde{V}_L}, \tag{10}$$

where $N_r > 0$ and $N_g > 0$ are the number of red and green cells at $\tilde{t} = 0$. Therefore, the initial radius is

$$\tilde{l}(0) = \frac{3(N_r + N_g) \tilde{V}_L}{4\pi}. \tag{11}$$

For oxygen, we assume the initial spheroid is sufficiently small that we have

$$\tilde{c}(\tilde{x}, 0) = \tilde{c}_0, \tag{12}$$

where $\tilde{c}_0 > 0$ is the external oxygen concentration.

We impose the following boundary conditions by assuming that the time rate of change of the spheroid radius, $d\tilde{l}(\tilde{t})/d\tilde{t}$, is given by the local velocity at the spheroid surface, and that the oxygen concentration at the spheroid surface is given by the external oxygen concentration,

$$\frac{d\tilde{l}}{d\tilde{t}} = \tilde{v}(\tilde{l}(\tilde{t}), \tilde{t}), \quad \tilde{c}(\tilde{l}(\tilde{t}), \tilde{t}) = \tilde{c}_0. \tag{13}$$

Lastly, we have a symmetry condition at the centre of the spheroid, $\tilde{x} = 0$,

$$\frac{\partial \tilde{c}(0, \tilde{t})}{\partial \tilde{x}} = 0, \quad \tilde{v}(0, \tilde{t}) = 0. \tag{14}$$

To solve the dimensional model we must specify values of fifteen free parameters, $(\tilde{V}_L, \tilde{V}_D, \tilde{D}, \tilde{\beta}, \tilde{\gamma}, \tilde{A}, \tilde{B}, \tilde{C}, m_1, m_2, m_3, \sigma, \tilde{c}_g, \tilde{c}_r, \tilde{c}_d)$, and four quantities relating to initial data, $(N_r, N_g, \tilde{l}(0), \tilde{c}_0)$. Given the large parameter space, we choose to implement the model in a nondimensional framework.

3.1 Nondimensionalisation

We introduce $x = \tilde{x}/\tilde{l}(0), t = \tilde{t}\tilde{A}, l(t) = \tilde{l}(t)/\tilde{l}(0), r = \tilde{r}\tilde{V}_L, g = \tilde{g}\tilde{V}_L$, and $c = \tilde{c}/\tilde{c}_0$ to arrive at a simplified nondimensional model,

$$\frac{\partial r}{\partial t} + v \frac{\partial r}{\partial x} = 2K_g(c)g - [b(c)g - d(c)r + K_r(c) + K_d(c)]r, \tag{15}$$

$$\frac{\partial g}{\partial t} + v \frac{\partial g}{\partial x} = K_r(c)r - [b(c)g - d(c)r + K_g(c) + K_d(c)]g, \tag{16}$$

$$\frac{1}{x^2} \frac{\partial}{\partial x} (x^2 v) = b(c)g - d(c)r, \tag{17}$$

$$\frac{1}{x^2} \frac{\partial}{\partial x} \left(x^2 \frac{\partial c}{\partial x} \right) = k(c)g + \gamma(c)r, \tag{18}$$

on $0 < x < l(t)$ and $t > 0$, where $b(c) = K_r(c) - d(c), d(c) = (1 - \delta)K_d(c), k(c) = \beta K_g(c) + \gamma(c), \delta = V_D/V_L, \beta = \tilde{l}^2(0)\tilde{A}\tilde{\beta}/(D c_0 V_L)$, and $\gamma(c) = \tilde{l}^2(0)\tilde{\gamma}(\tilde{c})/(D c_0 V_L)$. To arrive at Eq. (18) from Eq. (5), we make the usual quasi-steady-state assumption for oxygen (Greenspan 1972; Ward and King 1997).

The nondimensional kinetic rate functions are

$$K_g(c) = \frac{c^{m_1}}{c^{m_1} + c^{m_1}}, \tag{19}$$

$$K_r(c) = \frac{Bc^{m_2}}{c_r^{m_2} + c^{m_2}}, \tag{20}$$

$$K_d(c) = C \left(1 - \frac{\sigma c^{m_3}}{c_d^{m_3} + c^{m_3}} \right), \tag{21}$$

where $c_g = \tilde{c}_g/c_0, c_r = \tilde{c}_r/c_0, c_d = \tilde{c}_d/c_0, B = \tilde{B}/\tilde{A}$, and $C = \tilde{C}/\tilde{A}$. The initial and boundary conditions are given by

$$l(0) = 1, \quad c(x, 0) = 1, \quad r(x, 0) = \frac{N_r}{N_r + N_g}, \quad g(x, 0) = \frac{N_g}{N_r + N_g}, \tag{22}$$

$$\frac{dl}{dt} = v(l(t), t), \quad c(l(t), t) = 1, \quad \frac{\partial c(0, t)}{\partial x} = 0, \quad v(0, t) = 0. \tag{23}$$

Together, Eqs. (15)–(18) form a nonlinear moving boundary problem on $0 < x < l(t)$. We solve the model numerically by first transforming to a fixed domain. The terms associated with the advective transport are approximated using an upstream difference

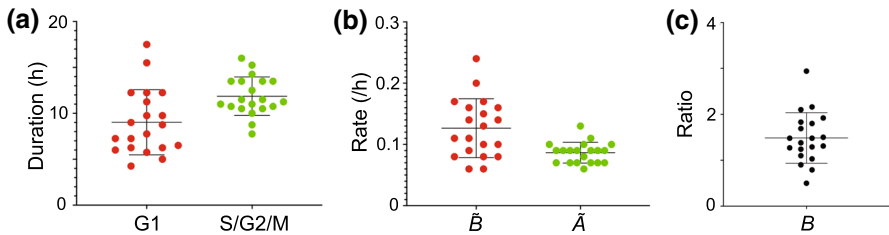


Fig. 4 (Colour Figure Online) Experimental measurements of cell cycle transition times for FUCCI-C8161 cells without oxygen limitation. **a** Durations of time spent in G1 (red) and S/G2/M (green) phases for twenty FUCCI-C8161 melanoma cells. **b** Estimates of \tilde{A} , the rate at which cells in S/G2/M (green) go through mitosis and transit into G1 (red), and estimates of \tilde{B} , the rate at which cells in G1 (red) enter the cell cycle and transit into S/G2/M (green) phase. **c** Estimates of $B = \tilde{B}/\tilde{A}$. Experimental data from Haass et al. (2014)

approximation, whereas terms associated with diffusive transport are approximated using a central difference approximation. The resulting system of nonlinear evolution equations are integrated through time using an implicit Euler approximation, leading to a system of nonlinear algebraic equations that are solved using Newton–Raphson iteration (Simpson et al. 2005). Full details of the numerical method are outlined in the Supplementary Material document; software programs written in MATLAB are available on GitHub.

In our experiments, such those illustrated in Figs. 1c and 3a, the initial spheroid radius $\tilde{l}(0) \approx 250 \mu\text{m}$. The characteristic timescale is related to the rate parameter \tilde{A} , which we can estimate by considering experimental data reported by Haass et al. (2014) who make careful measurements of the duration that C8161 melanoma cells fluoresce red and green in 2D culture where oxygen is plentiful. Data in Fig. 4a show estimates of the duration of time C8161 cells spend in G1 (red) and S/G2/M (green) phase for 20 individual cells. Taking the reciprocal of each recorded duration, we obtain estimates of \tilde{A} and \tilde{B} . Data in Fig. 4b suggest that $0.08 < \tilde{A} < 0.25 /\text{h}$ and $0.08 < \tilde{B} < 0.12 /\text{h}$. For simplicity, we take a representative estimate of $\tilde{A} \approx 0.1 /\text{h}$, which means that each unit duration of time in the nondimensional model corresponds to 10 h in the experiment. Given our estimates of \tilde{A} and \tilde{B} , we also estimate $B = \tilde{B}/\tilde{A}$, as shown in Fig. 4c, for which we can take a representative estimate of $B = 1.5$. Cell cycle duration estimates differ from cell line to cell line (Haass et al. 2014). Therefore, given this kind of duration data, we could follow a similar procedure to arrive at different estimates of \tilde{A} and \tilde{B} for different cell lines as appropriate.

4 Results and Discussion

This section explores the capability of the mathematical model to describe important features of tumour spheroids with FUCCI labelling. This investigation is performed through numerical investigation of various solutions of Eqs. (15)–(18). The aim of this investigation is not to undertake a detailed parameter estimation exercise, but rather to explore whether the mathematical model, Eqs. (15)–(18), can replicate key biological features of FUCCI-labelled spheroids. Sections 4.1–4.2 explore a series of

control experiments by using the mathematical model to replicate various experimental observations, across two different cell lines, in the absence of cell cycle inhibitors (Haass et al. 2014; Spoerri et al. 2020). Section 4.3 explores how to model *intervention* experiments by using the mathematical model to replicate spheroid growth in the presence of a cell cycle inhibiting drug (Beaumont et al. 2016; Haass et al. 2014; Haass and Gabrielli 2017; Vittadello et al. 2020).

4.1 Capturing Intratumoural Heterogeneity in a Single Cell Line

Experimental images in Fig. 2a–c illustrate that the spheroid radius increases by a factor of approximately 1.3 over 24 h. Over this timescale, the intratumoural structure evolves from a relatively homogeneous mixture of G1 (red) and S/G2/M (green) cells at the beginning of the experiment to eventually form a complex structure comprising: (i) a necrotic core at the centre of the spheroid; (ii) an intermediate spherical shell containing live quiescent cells arrested in the G1 (red) phase; and (iii) an outer-most region composed of a mixture of freely proliferating G1 (red) and S/G2/M (green) cells. In our numerical explorations, we seek to replicate these spatial and temporal patterns. For simplicity, we always set $m_1 = m_2 = m_3$, and $\gamma(c) = 0$, and assume that the initial spheroid is composed of an equal proportion of G2 (red) and S/G2/M (green) cells by setting $r(x, 0) = g(x, 0) = 0.5$. A MATLAB implementation of the numerical code is available on GitHub so that readers can explore the impact of choosing different parameter values.

We first explore numerical solutions of Eqs. (15)–(18) with parameter values summarised in Table 1 that give rise to the three kinetic rate functions shown in Fig. 5a. In this case, $K_g(c)$ and $K_r(c)$ rapidly increase to their maximum rates, unity and B , respectively, as c increases beyond the critical oxygen thresholds, c_r and c_g , respectively. Similarly, $K_d(c)$ rapidly decreases to $C(1 - \sigma)$ as c increases beyond the critical oxygen level c_d . The visual depiction of the kinetic rate functions show that $K_r(c) > K_g(c)$ for all c , so that the rate of G1 to S/G2/M transition is greater than the rate of S/G2/M to G1 transition. When oxygen is sufficiently reduced we have $K_d(c) > K_r(c) > K_g(c)$, which means that cell death is the dominant kinetic mechanism under these conditions. With these parameter choices, we plot the evolution of $r(x, t)$, $g(x, t)$, $c(x, t)$, $v(x, t)$, and $l(t)$ in Fig. 6a–c, where density and velocity profiles are plotted at $t = 1.2, 1.8$, and 2.4 . These nondimensional times correspond to 12, 18, and 24 h, respectively, in the real experiment. Profiles in Fig. 6a show that the spheroid grows with time and that both $g(x, t)$ and $r(x, t)$ are increasing functions of position, with the maximum volume fraction of living cells at the spheroid surface, $x = l(t)$, and a minimum at the centre of the spheroid, $x = 0$. Profiles of $c(x, t)$ also show that the oxygen concentration is an increasing function of x , which is consistent with oxygen diffusing into the spheroid from the free boundary at $x = l(t)$, while simultaneously consumed by living cells. Comparing the profiles of $r(x, t)$, $g(x, t)$, and $c(x, t)$, we see that by $t = 2.4$ we have almost a complete absence of living cells in the central region, indicating the eventual formation of a necrotic core, where $x < 0.8$.

An interesting feature of the solution in Fig. 6a is that the spatial distribution of living cells involves two subpopulations where $r(x, t) \approx g(x, t)$ at all locations, at all

Table 1 Parameter values

Parameter	Figure 6a	Figure 6b	Figure 8d Cell type 1	Figure 8d Cell type 2	Figure 9a–c	Figure 9d–f
σ	1.0	1.0	1.0	1.0	1.0	1.0
δ	0.9	0.9	0.9	0.9	0.9	0.9
β	15.0	15.0	10.0	10.0	10.0	10.0
c_r	0.1	0.7	0.9	0.7	0.7	0.7
c_g	0.1	0.1	0.1	0.1	0.1	0.1
c_d	0.5	0.5	0.5	0.5	0.5	0.5
m_1	10.0	10.0	3.0	6.0	10.0	10.0
m_2	10.0	10.0	3.0	6.0	10.0	10.0
m_3	10.0	10.0	3.0	6.0	10.0	10.0
B	1.5	1.5	1.0	3.0	1.5	1.5
C	1.8	1.8	1.8	1.8	1.8	1.8
$\gamma(c)$	0.0	0.0	0.0	0.0	0.0	0.0
λ	N/A	N/A	N/A	N/A	N/A	10.0
t_d	N/A	N/A	N/A	N/A	N/A	7.2

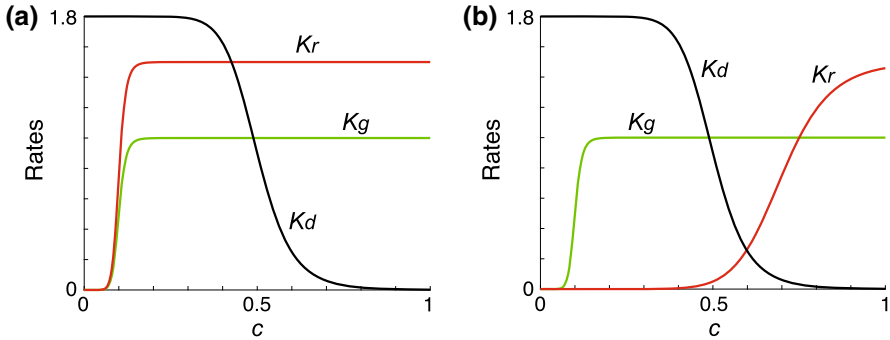


Fig. 5 (Color Figure Online) Kinetic rate functions $K_r(c)$, $K_g(c)$, and $K_d(c)$. **a** $c_r = c_g = 0.1$. **b** $c_r = 0.7$, $c_g = 0.1$, such that both $K_r(c)$ and $K_d(c)$ functions in **a** and **b** are identical. In both sets of profiles we have $B = 1.5$, $C = 1.8$, $c_d = 0.5$, $m_1 = m_2 = m_3 = 10$

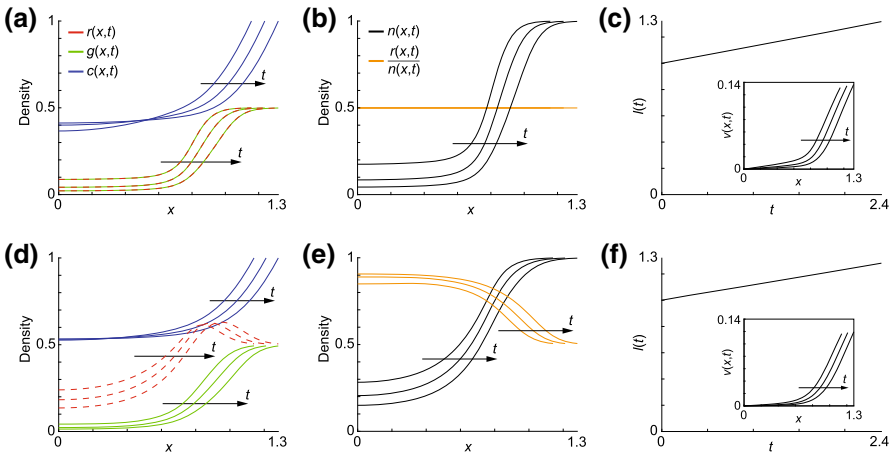


Fig. 6 (Color Figure Online) Numerical solutions of Eqs. (15)–(18) $t = 1.2, 1.8$, and 2.4 . **a, d** Solutions $r(x, t)$, $g(x, t)$, and $c(x, t)$, with the direction of increasing t indicated by the arrow. **b, e** Solutions $n(x, t) = r(x, t) + g(x, t)$ and $r(x, t)/n(x, t)$ as indicated. **c, f** Time evolution of spheroid radius, $l(t)$, with the inset showing the velocity profile, $v(x, t)$. Solutions in **a–c** correspond to the kinetic rate parameters in Fig. 5a, while solutions in **d–f** correspond to the kinetic rate parameters in Fig. 5b

times considered. Therefore, for this choice of parameters, while we do see the eventual formation of a necrotic core, we do not see the formation of an intermediate zone of G1-arrested cells like in Fig. 2c. This observation is clear when we plot the proportion of G1 cells, $r(x, t)/n(x, t)$ in Fig. 6b, where we have $r(x, t)/n(x, t) = 0.5$ for all x , at all times considered. We visualise the cell velocity, $v(x, t)$, in Fig. 6c showing that we have $v(x, t) > 0$ for all x during the experiment, indicating that the total volume gain through proliferation exceeds the volume loss through cell death. This gain in volume leads to $l(2.4) \approx 1.3$, which is consistent with the rate of expansion of the experimental spheroid in Fig. 2a–c over the same time interval.

To emphasise the key features of this solution of Eqs. (15)–(18) we now summarise the solution from Fig. 6a in a different format in Fig. 7a, by plotting $r(x, t)$, $g(x, t)$,

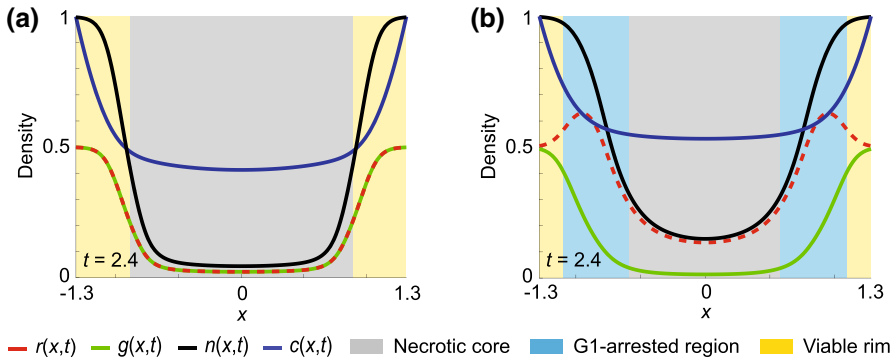


Fig. 7 (Color Figure Online) Visualisation of the predicted intratumoural structure. **a, b** show profiles of $r(x, t)$, $g(x, t)$, $n(x, t)$, and $c(x, t)$ at $t = 2.4$, on $-l(t) < x < l(t)$, with different intratumoural substructures highlighted by different colours. In particular we highlight the regions corresponding to the necrotic core, the intermediate G1-arrested quiescent zone and the freely-proliferating outer-rim. Results in **a, b** correspond to the parameter choice in Fig. 6a–c and d–f, respectively

$n(x, t)$, and $c(x, t)$ at the end of the experiment, $t = 2.4$, on $-l(t) < x < l(t)$. Plotting the solution in this format helps to emphasise that the mathematical model can predict the formation of different intratumoural heterogeneity within the spheroid, as revealed by FUCCI labelling. We note that similar to Ward and King’s model, solutions of our model are continuous so that the internal boundaries between the three regions are not well defined. In Fig. 7a, we see that the distribution of $n(x, t)$ and $g(x, t)$ is such that an extensive central necrotic core develops, where $|x| < 0.8$, with very low density of living cells in the central region of the spheroid. In contrast, the outer region of the spheroid, where $|x| > 0.8$, is composed of freely proliferating cells with $g(x, t) \approx r(x, t)$. Within this outer-most regions there are no obvious spatial patterns of cell cycle status.

Our initial numerical results in Fig. 6a–c are qualitatively consistent with the evolution of the spheroid size, $l(t)$, measured in Fig. 2. The intratumoural structure is very different since the numerical solution in Fig. 6a–c does not involve any intermediate G1-arrested region as is clear in Fig. 2b, c. To incorporate this phenomenon, we resolve the model with $c_r = 0.7$ and $c_g = 0.1$, and all other parameters unchanged. The kinetic rate functions are shown in Fig. 5b in which we see that: (i) $K_d(c) > K_g(c) > K_r(c)$ for sufficiently small oxygen concentrations; (ii) $K_g(c) > K_d(c) > K_r(c)$ at intermediate oxygen concentrations; and (iii) $K_r(c) > K_g(c) > K_d(c)$ at sufficiently large oxygen concentrations. The associated numerical solutions of Eqs. (15)–(18) are shown in Fig. 6d–f. Comparing profiles in Fig. 6a, d indicates that we now have a very different intratumoural structure. Similar to before, we see that $g(x, t)$ and $c(x, t)$ are increasing functions of x , whereas $r(x, t)$ is more complicated since there is a local maximum in $r(x, t)$ within the spheroid. Interestingly, comparing the profiles of $n(x, t)$ in Fig. 6b, e we see that the spatial distribution of the total live cell density is very similar for these two choices of parameters, yet the internal structure of the spheroids, as revealed by FUCCI-labelling in our theoretical model, is very different. The velocity profiles and the time evolution of the outer radius of the spheroid is shown

in Fig. 6f, where again we see that the velocity field and the evolution of the outer spheroid radius is very similar for these two choices of model parameters.

The profile in Fig. 7b highlights the intratumoural structure by plotting $r(x, t)$, $g(x, t)$, $n(x, t)$, and $c(x, t)$ at the end of the experiment, $t = 2.4$, on $-l(t) < x < l(t)$. In this case, we see that the internal structure defined by the distribution of various cell populations includes: (i) the necrotic core for $|x| < 0.6$; (ii) an intermediate region composed of G1-arrested (red) living cells for $0.6 < |x| < 1.1$; and, (iii) an outer-most rim of freely proliferating cells for $1.1 < |x| < 1.3$. This exercise of comparing results in Fig. 6a–c and d–f shows that the mathematical model we have developed can replicate key features of 3D tumour spheroid models with intratumoural heterogeneity revealed by FUCCI labelling. These differences are visually pronounced when we plot those results in Fig. 7 where we deliberately highlight regions within the spheroid according to the proliferation status.

4.2 Capturing Intratumoural Heterogeneity Across Multiple Cell Lines

Numerical results in Figs. 6 and 7 show that our model is able to capture both the time evolution of the spheroid size, as well as the fundamental intratumoural structure regarding the status of the cell cycle at different positions within the spheroid for a single cell line, in this case the C8161 melanoma cell line. We now further explore the capacity of the model to represent different forms of intratumoural structure as revealed by FUCCI labelling in different cell lines. Recent experimental data reported by Spoerri et al. (2020) describe a range of melanoma spheroids constructed using different cell lines and characterise the proliferative heterogeneity calculating the percentage of G1-labelled (red) cells as a function of distance from spheroid's surface. In our model, we use the standard spherical coordinate system, $0 < x < l(t)$, so that x is the radial position measured relative to the centre of the spheroid. Spoerri et al. (2020) measures the distance from the surface of the spheroid, $X = l(t) - x$, so that $X = 0$ is at the surface, and $X = l(t)$ is at the centre of the spheroid. Data reported by Spoerri et al. (2020) show the proportion of G1-labelled cells as a function of X gives rise to a range of cell line-specific profiles. Images in Fig. 8a, b show melanoma spheroids with FUCCI labelling, using two different melanoma cell lines: WM164 cells in Fig. 8a and C8161 cells in Fig. 8b.

We show, schematically, the observed trends in terms of the proportion of G1-labelled cells as a function of X in Fig. 8c, d. For the WM164 cell line, we see that the G1-labelled cells make up approximately 75 % of the total living population at the spheroid surface, and the proportion of G1-labelled cells increases gradually with X . In contrast, for the C8161 cell line, the proportion of G1-labelled cells is approximately 45 % of the total living population at the spheroid surface, and we see a far more rapid increase in the proportion of G1-labelled cells with X . These measurements are consistent with our visual interpretation of the spheroids in Fig. 8a, b where we see that the WM164 spheroid does not contain a visually distinct necrotic core, whereas the C8161 spheroid develops a very clear necrotic core. Results in 8d show numerical solutions of Eqs. (15)–(18) that qualitatively model the WM164 and C8161 spheroids, respectively. We obtain the solution of Eqs. (15)–(18), for the parameter values in Table

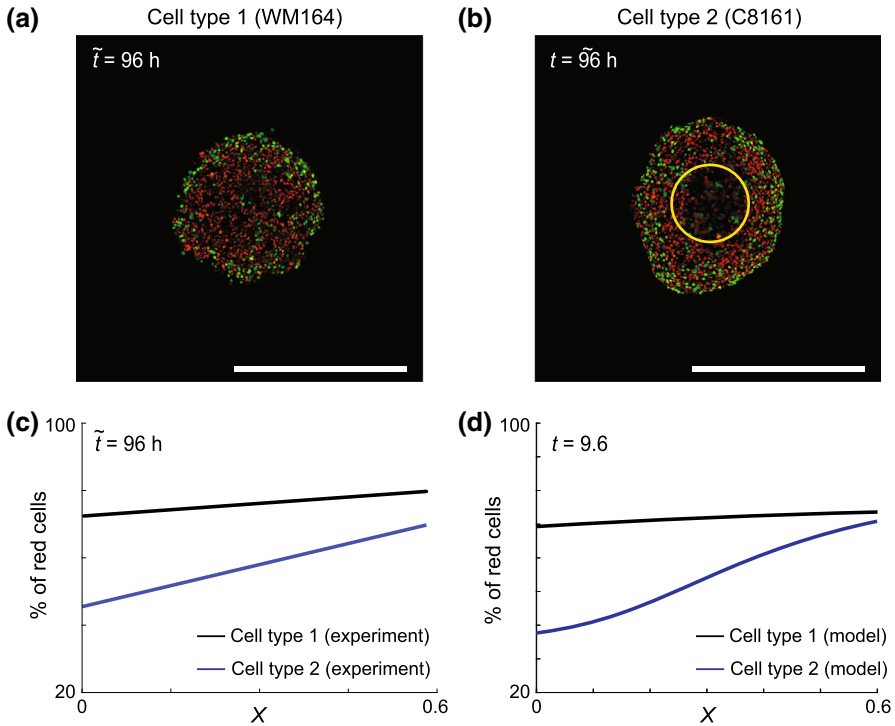


Fig. 8 Comparison of experimental data and model predictions. **a, b** Confocal microscopy images of tumour spheroids after 96 h derived from two different cell types. The scale bar corresponds to 550 μm . **c, d** Schematics showing different profiles of the percentage of red cells within the spheroids superimposed with numerical results from the model with parameter values in Table 1

1, at $t = 9.6$, and we plot $100 \times r(X, t)/n(X, t) \%$, which qualitatively matches the intratumoural heterogeneity reported by Spoerri et al. (2020). This modelling exercise confirms that the mathematical model is sufficiently flexible that it can be used to model the experimental data reported by Spoerri et al. (2020).

4.3 Simulating the Action of Anti-mitotic Drugs

In Sects. 4.1–4.2, we focus on using the mathematical model to replicate and visualise spatial patterns of cell cycle status within a growing spheroid under control conditions. One of the key reasons that 3D spheroid cultures are of high interest in the experimental cancer cell research community is the ability to test different potential anti-cancer drug treatments in a realistic 3D geometry (Friedrich et al. 2009; Loessner et al. 2013). Various anti-mitotic drugs have been developed and applied to 3D spheroid cultures (e.g. Crivelli et al. 2012; Haass et al. 2008; Loessner et al. 2013; Smalley et al. 2008; Stehn et al. 2013), and with the development of FUCCI-labelling we have vastly improved opportunities to visualise how such drug treatments impact the spatial distribution of cell cycle status within the treated spheroid (Haass et al. 2014;

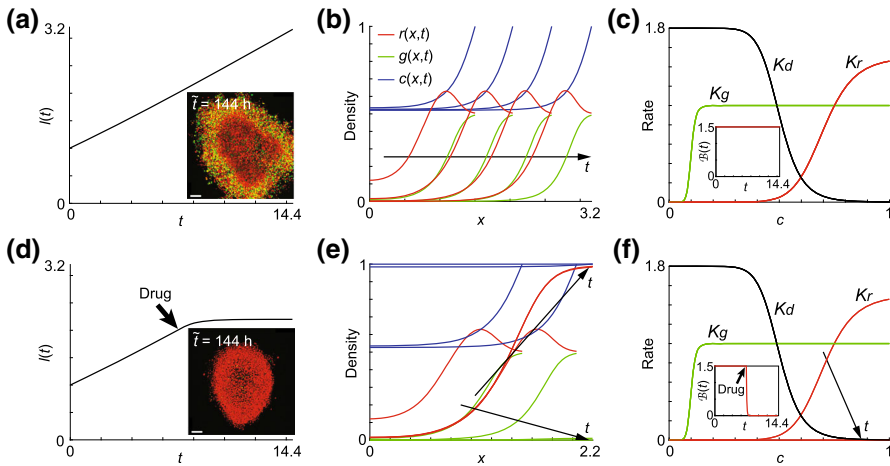


Fig. 9 (Color Figure Online) Numerical simulation describing the application of an anti-mitotic drug. **a–c** Control tumour spheroid growth without treatment. **d–f** Treated tumour spheroid with the drug applied at $t = 7.2$. **a, d** Simulated time evolution of $l(t)$ in the control and treated simulations, respectively. The insets show the experimental images of C8161-FUCCI melanoma spheroids at day six. The scale bar corresponds to $110 \mu\text{m}$. **b, e** Simulated profiles of $r(x, t)$, $g(x, t)$, and $c(x, t)$ at $t = 3.6, 7.2, 10.8$, and 14.4 with arrows showing the direction of increasing time. **c, f** Kinetic rate functions for the control and simulated spheroids, respectively. The insets show $B(t)$, indicating how the drug is applied to the simulations

Beaumont et al. 2016; Kienzle et al. 2017). The experimental images in Fig. 9a, d show a control C8161 melanoma spheroid, and a U0126-treated C8161 melanoma spheroid, after six days, respectively. In this case, both the control and treatment spheroids are grown for three days initially, and U0126 is applied at day three to the treatment group. U0126 is a MEK-inhibitor that leads to G1 arrest (Haass et al. 2014; Smalley et al. 2008). Comparing the images in Fig. 9a, d leads to two obvious conclusions: (i) the treated spheroid is almost completely composed of G1-arrested (red) cells; and, (ii) the size of the treated spheroid is smaller than the untreated spheroid.

To incorporate the effect U0126 in our model, we make the straightforward assumption that the drug affects the maximum rate at which cells transition from G1 phase (red) to S/G2/M phase (green) by modifying the appropriate kinetic function,

$$K_r(c) = \frac{B(t)c^{m_2}}{c_r^{m_2} + c^{m_2}}, \tag{24}$$

with

$$B(t) = \begin{cases} B & \text{if } t < t_d \\ B e^{-\lambda(t-t_d)} & \text{if } t \geq t_d. \end{cases} \tag{25}$$

Here, t_d is the time that the drug is applied, and $\lambda > 0$ is an intrinsic drug-sensitivity parameter (Enderling and Chaplain 2014; Lewin et al. 2018). Our choice of the functional form of $B(t)$ is not unique and could vary depending on the particular cell line

and the particular drug treatment (Collis et al. 2017; Crivelli et al. 2012; de Pillis et al. 2006).

We simulate these experiments by setting $t_d = 7.2$ and $\lambda = 10$ and summarise our numerical results in Fig. 9. Comparing profiles in Fig. 9a, d we see that the control and treatment experiments are indistinguishable for $t < t_d$, as expected. For $t > t_d$ we see a clear reduction in the time rate of change of radius, $l(t)$, in the treated spheroid. The treated tumour has almost stopped growing at the end of the simulation, whereas the untreated spheroid continues to grow at an almost constant rate of radial expansion. The density profiles in Fig. 9b show that the control spheroid rapidly develops a necrotic core, and that the populations of live cells continues to expand over time. In comparison, the density profiles in Fig. 9e show that after the application of the drug we observe a rapid decline in $g(x, t)$ throughout the spheroid, and the total population becomes dominated by cells in G1 phase, $r(x, t)$. Note that the density profiles in Fig. 9b, e are plotted on different spatial scales so that the differences in intratumoural structure is clear, emphasising that the solutions of the mathematical model qualitatively capture the key experimental observations. The associated kinetic rate functions for these simulations are summarised in Fig. 9c, f, with the drug treatment summarised by the function $\mathcal{B}(t)$, shown as an inset in both subfigures.

5 Conclusion and Outlook

In this work, we develop a mathematical model of 3D tumour spheroid growth that is compatible with FUCCI-labelling, which highlights the spatial location of cells in terms of their cell cycle status. In these experiments, cells in G1 phase fluoresce red, while cells in S/G2/M phase fluoresce green. Traditional tumour spheroid experiments do not provide spatio-temporal information about the cell cycle status, and it is not obvious whether all living cells are freely cycling or not. Our experiments show that FUCCI provides detailed insight into the development of intratumoural heterogeneity as the spheroid grows. In particular, at late time points we see: (i) a necrotic region in the centre of the spheroid that does not contain living fluorescent cells; (ii) an intermediate spherical shell composed of living G1-arrested (red) cells; and (iii) an outer spherical shell composed of a mixture of freely cycling G1 (red) and S/G2/M (green) cells. We demonstrate how to incorporate this information into a model of 3D tumour spheroids by adapting the well-known model of Ward and King (1997) to include three subpopulations of cells: (i) cells in G1 phase, $r(x, t)$; (ii) cells in G2/S/M phase, $g(x, t)$, and (iii) dead cells $m(x, t)$. In this framework, cells move with the local velocity field, $v(x, t)$, and the transitions between the G1 and G2/S/M phases are consistent with FUCCI-labelling. Rates of cell death and time points of transition through the cell cycle are taken as functions of the local oxygen concentration. Further, we consider oxygen to diffuse into the spheroid from the free surface, while being simultaneously consumed by the living cells. We show how to partially parameterise the mathematical model using experimental observations, and we explore numerical solutions of the nonlinear moving boundary problem and show that this model can capture key features of intratumoural heterogeneity in a single cell line, differences in

intratumoural heterogeneity across multiple cell lines, as well as being able to mimic spheroid growth in the presence of anti-mitotic drugs.

There are many opportunities for further generalisation of this work, both experimentally and theoretically. From a modelling perspective, one of the key assumptions we make in modelling FUCCI is that we consider the total live population to be composed of cells in G1 phase (red) and cells in S/G2/M phase (green). In reality, it is also possible to identify further groupings based on FUCCI labelling. For example, cells in which both the red and green fluorescence are active appear yellow, and these cells are often considered to be in early S phase (Haass et al. 2014). Under these conditions, we would consider the living population to be composed of three groups of cells: G1 phase (red), eS phase (yellow), and S/G2/M phase (green). Extending our model to deal with this additional phase would involve reformulating the mathematical model to describe three densities of living cells and one density of dead cells. This extended model would be able to capture additional biological features, but this benefit comes with the cost of incorporating a greater number of model parameters need to be estimated. Further modelling refinements could include introducing additional necrotic depletion mechanisms Ward and King (1999), as well as allowing different groups of cells to experience different transport velocities. While the mathematical extensions required to incorporate these extensions are conceptually and computationally straightforward, our ability to parameterise such extended models is less clear without gathering additional experimental data and so we leave these extensions for future consideration (Simpson et al. 2020). Another opportunity for further investigation is the analysis of travelling wave solutions of Eqs. (15)–(18). In their original work, Ward and King (1997) were able to make progress in interpreting their model in terms of travelling wave analysis in the limit that the exponents in the Hill function become infinitely large and the kinetic rate functions simplify to Heaviside functions. We anticipate that a similar analysis could be considered for our more complicated model, and we leave this analysis for future consideration. From an experimental perspective, we note that all experimental images and data discussed in this work relate to tumour spheroids composed of melanoma cells. We anticipate that our model and modelling framework will also be relevant to spheroids made from other types of cancer cell lines transduced with FUCCI system. As already noted, our experimental motivation involves the traditional FUCCI system with two fluorescent colours, which motivates us to consider the living cells as being composed of two subpopulations. More recent experimental technology, FUCCI4 (Bajar et al. 2016), uses four fluorescent colours to label the cell cycle. We expect that our approach here could be developed further by considering the live cell population to be given by the sum of four densities that correspond to the colours associated with FUCCI4 labelling.

Supplementary Information The online version contains supplementary material available at <https://doi.org/10.1007/s11538-021-00878-4>.

Acknowledgements MJS and NKH are supported by the Australian Research Council (DP200100177). NKH is supported by the National Health and Medical Research Council (APP1084893). WJ is supported by a QUT Vice-Chancellor's Research Fellowship. We thank two referees and Emeritus Professor Sean McElwain for their helpful suggestions.

References

- Bajar BT, Lam AJ, Badiie RK, Oh Y-H, Chu J, Zhou XX, Kim N, Kim BB, Chung M, Yablonovitch AL, Cruz BF, Kulalert K, Tao JJ, Meyer T, Su X-D, Lin M-Z (2016) Fluorescent indicators for simultaneous reporting of all four cell cycle phases. *Nat Methods* 13:993–996. <https://doi.org/10.1038/nmeth.4045>
- Beaumont KA, Mohana-Kumaran N, Haass NK (2014) Modeling melanoma in vitro and in vivo. *Healthcare* 2:27–46. <https://doi.org/10.3390/healthcare2010027>
- Beaumont KA, Hill DS, Daignault SM, Lui GY, Sharp DM, Gabrielli B, Weninger W, Haass NK (2016) Cell cycle phase-specific drug resistance as an escape mechanism of melanoma cells. *J Investig Dermatol* 136:1479–1489. <https://doi.org/10.1016/j.jid.2016.02.805>
- Breward CJ, Byrne HM, Lewis CE (2002) The role of cell–cell interactions in a two-phase model for avascular tumour growth. *J Math Biol* 45:125–152. <https://doi.org/10.1007/s002850200149>
- Byrne HM, King JR, McElwain DLS, Preziosi L (2003) A two-phase model of solid tumour growth. *Appl Math Lett* 16:567–573. [https://doi.org/10.1016/S0893-9659\(03\)00038-7](https://doi.org/10.1016/S0893-9659(03)00038-7)
- Chan FK, Shisler J, Bixby JG, Felices M, Zheng L, Appel M, Orenstein J, Moss B, Lenardo MJ (2003) A role for tumor necrosis factor receptor-2 and receptor-interacting protein in programmed necrosis and antiviral responses. *J Biol Chem* 278:51613–51621. <https://doi.org/10.1074/jbc.M305633200>
- Chaplain MA, Graziano L, Preziosi L (2006) Mathematical modelling of the loss of tissue compression responsiveness and its role in solid tumour development. *Math Med Biol* 23:197–229. <https://doi.org/10.1093/imammb/dql009>
- Collis J, Hubbard ME, O’Dea RD (2016) Computational modelling of multiscale, multiphase fluid mixtures with application to tumour growth. *Comput Methods Appl Mech Eng* 309:554–578. <https://doi.org/10.1016/j.cma.2016.06.015>
- Collis J, Hubbard ME, O’Dea RD (2017) A multi-scale analysis of drug transport and response for a multi-phase tumour model. *Eur J Appl Math* 28:499–534. <https://doi.org/10.1017/S0956792516000413>
- Crivelli JJ, Földes J, Kim PS, Wares JR (2012) A mathematical model for cell cycle-specific cancer virotherapy. *J Biol Dyn* 6:104–120. <https://doi.org/10.1080/17513758.2011.613486>
- Deakin AS (1975) Model for the growth of a solid in vitro tumor. *Growth* 39:159–165
- de Pillis LG, Gu W, Radunskaya AE (2006) Mixed immunotherapy and chemotherapy of tumors: modeling, applications and biological interpretations. *J Theor Biol* 238:841–862. <https://doi.org/10.1016/j.jtbi.2005.06.037>
- Enderling H, Chaplain MAJ (2014) Mathematical modeling of tumor growth and treatment. *Curr Pharm Des* 20:4934–4940
- Flegg JA, Nataraj N (2019) Mathematical modelling and avascular tumour growth. *Resonance* 24:313–325. <https://doi.org/10.1007/s12045-019-0782-8>
- Friedrich J, Seidel C, Ebner R, Kunz-Schughart LA (2009) Spheroid-based drug screen: considerations and practical approach. *Nat Protoc* 4:309–324. <https://doi.org/10.1038/nprot.2008.226>
- Greenspan HP (1972) Models for the growth of a solid tumor by diffusion. *Stud Appl Math* 51:317–340. <https://doi.org/10.1002/sapm1972514317>
- Haass NK, Sproesser K, Nguyen TK, Contractor R, Medina CA, Nathanson KL, Herlyn M, Smalley KSM (2008) The mitogen-activated protein/extracellular signal-regulated kinase kinase inhibitor AZD6244 (ARRY-142886) induces growth arrest in melanoma cells and tumor regression when combined with docetaxel. *Clin Cancer Res* 14:230–239. <https://doi.org/10.1158/1078-0432.CCR-07-1440>
- Haass NK, Beaumont KA, Hill DS, Anfosso A, Mrass P, Munoz MA, Kinjyo I, Weninger W (2014) Real-time cell cycle imaging during melanoma growth, invasion, and drug response. *Pigment Cell Melanoma Res* 27:764–776. <https://doi.org/10.1111/pcmr.12274>
- Haass NK, Gabrielli B (2017) Cell cycle-tailored targeting of metastatic melanoma: challenges and opportunities. *Exp Dermatol* 26:649–655. <https://doi.org/10.1111/exd.13303>
- Jin W, Shah ET, Penington CJ, McCue SW, Chopin LK, Simpson MJ (2016) Reproducibility of scratch assays is affected by the initial degree of confluence: experiments, modelling and model selection. *J Theor Biol* 390:136–145. <https://doi.org/10.1016/j.jtbi.2015.10.040>
- Jin W, Shah ET, Penington CJ, McCue SW, Maini PK, Simpson MJ (2017) Logistic proliferation of cells in scratch assays is delayed. *Bull Math Biol* 79:1028–1050. <https://doi.org/10.1007/s11538-017-0267-4>
- Jin W, McCue SW, Simpson MJ (2019) Extended logistic growth model for heterogeneous populations. *J Theor Biol* 445:51–61. <https://doi.org/10.1016/j.jtbi.2018.02.027>

- Kienzle A, Kurch S, Schlöder J, Berges C, Ose R, Schupp J, Tuettenberg A, Weiss H, Schultze J, Winzen S, Schinnerer M, Koynov K, Mezger M, Haass NK, Tremel W, Jonuleit H (2017) Dendritic mesoporous silica nanoparticles for pH-stimuli-responsive drug delivery of TNF- α . *Adv Healthc Mater* 6:1700012. <https://doi.org/10.1002/adhm.201700012>
- Kunz-Schughart LA, Kreutz M, Knuechel R (1998) Multicellular spheroids: a three-dimensional in vitro culture system to study tumour biology. *Int J Exp Pathol* 79:1–23. <https://doi.org/10.1046/j.1365-2613.1998.00051.x>
- Landman KA, Please CP (2001) Tumour dynamics and necrosis: surface tension and stability. *Math Med Biol* 18:131–158. <https://doi.org/10.1093/imammb/18.2.131>
- Lewin TD, Maini PK, Moros EG, Enderling H, Byrne HM (2018) The evolution of tumour composition during fractionated radiotherapy: implications for outcome. *Bull Math Biol* 80:1207–1235. <https://doi.org/10.1007/s11538-018-0391-9>
- Lewin TD, Maini PK, Moros EG, Enderling H, Byrne HM (2020) A three phase model to investigate the effects of dead material on the growth of avascular tumours. *Math Model Nat Phenom* 15:22. <https://doi.org/10.1051/mmnp/2019039>
- Loessner D, Flegg JA, Byrne HM, Clements JA, Huttmacher DW (2013) Growth of confined cancer spheroids: a combined experimental and mathematical modelling approach. *Integr Biol* 5:597–605. <https://doi.org/10.1039/c3ib20252f>
- Maeda S, Wada H, Naito Y, Nagano H, Simmons S, Kagawa Y, Naito A, Kikuta J, Ishii T, Tomimaru Y, Hama N, Kawamoto K, Kobayashi S, Eguchi H, Umeshita K, Ishii H, Doki Y, Mori M, Ishii M (2014) Interferon- α acts on the S/G2/M phases to induce apoptosis in the G1 phase of an IFNAR2-expressing hepatocellular carcinoma cell line. *J Biol Chem* 289:23786–23795. <https://doi.org/10.1074/jbc.M114.551879>
- Maini PK, McElwain DLS, Leavesley DI (2004) Traveling wave model to interpret a wound-healing cell migration assay for human peritoneal mesothelial cells. *Tissue Eng* 10:475–482. <https://doi.org/10.1089/107632704323061834>
- Maini PK, McElwain DLS, Leavesley D (2004) Travelling waves in a wound healing assay. *Appl Math Lett* 17:575–580. [https://doi.org/10.1016/S0893-9659\(04\)90128-0](https://doi.org/10.1016/S0893-9659(04)90128-0)
- McElwain DLS, Morris LE (1978) Apoptosis as a volume loss mechanism in mathematical models of solid tumor growth. *Math Biosci* 39:147–157. [https://doi.org/10.1016/0025-5564\(78\)90033-0](https://doi.org/10.1016/0025-5564(78)90033-0)
- McElwain DLS, Calcott R, Morris LE (1979) A model of vascular compression in solid tumours. *J Theor Biol* 78:405–415. [https://doi.org/10.1016/0022-5193\(79\)90339-4](https://doi.org/10.1016/0022-5193(79)90339-4)
- Nath S, Devi GR (2016) Three-dimensional culture systems in cancer research: focus on tumor spheroid model. *Pharmacol Ther* 163:94–108. <https://doi.org/10.1016/j.pharmthera.2016.03.013>
- Norton L, Simon R, Brereton HD, Bogden AE (1976) Predicting the course of Gompertzian growth. *Nature* 264:542–545. <https://doi.org/10.1038/264542a0>
- Pettet GJ, Please CP, Tindall MJ, McElwain DLS (2001) The migration of cells in multicell tumor spheroids. *Bull Math Biol* 63:231–257. <https://doi.org/10.1006/bulm.2000.0217>
- Sakaue-Sawano A, Kurokawa H, Morimura T, Hanyu A, Hama H, Osawa H, Kashiwagi S, Fukami K, Miyata T, Miyoshi H, Imamura T, Ogawa M, Masai H, Miyawaki A (2008) Visualizing spatiotemporal dynamics of multicellular cell-cycle progression. *Cell* 132:487–498. <https://doi.org/10.1016/j.cell.2007.12.033>
- Santini MT, Rainaldi G (1999) Three-dimensional spheroid model in tumor biology. *Pathobiology* 67:148–157. <https://doi.org/10.1159/000028065>
- Sarapata EA, de Pillis LG (2014) A comparison and catalog of intrinsic tumor growth models. *Bull Math Biol* 76:2010–2024. <https://doi.org/10.1007/s11538-014-9986-y>
- Simpson MJ, Landman KA, Clement TP (2005) Assessment of a non-traditional operator split algorithm for simulation of reactive transport. *Math Comput Simul* 70:44–60. <https://doi.org/10.1016/j.matcom.2005.03.019>
- Simpson MJ, Jin W, Vittadello ST, Tambyah TA, Ryan JM, Gunasingh G, Haass NK, McCue SW (2018) Stochastic models of cell invasion with fluorescent cell cycle indicators. *Phys A Stat Mech Its Appl* 510:375–386. <https://doi.org/10.1016/j.physa.2018.06.128>
- Simpson MJ, Baker RE, Vittadello ST, Maclaren OJ (2020) Parameter identifiability analysis for spatiotemporal models of cell invasion. *J R Soc Interface* 17:20200055. <https://doi.org/10.1098/rsif.2020.0055>
- Smalley KS, Lioni M, Noma K, Haass NK, Herlyn M (2008) In vitro three-dimensional tumor microenvironment models for anticancer drug discovery. *Expert Opin Drug Discov* 3:1–10. <https://doi.org/10.1517/17460441.3.1.1>

- Spill F, Andasari V, Mak M, Kamm RD, Zaman MH (2016) Effects of 3D geometries on cellular gradient sensing and polarization. *Phys Biol* 13:036008. <https://doi.org/10.1088/1478-3975/13/3/036008>
- Spoerri L, Beaumont KA, Anfosso A, Haass NK (2017) Real-time cell cycle imaging in a 3D cell culture model of melanoma. In: 3D cell culture. Humana Press, New York, NY, pp 401–416. https://doi.org/10.1007/978-1-4939-7021-6_29
- Spoerri L, Tonnesen-Murray CA, Gunasingh G, Hill DS, Beaumont KA, Jurek RJ, Vanwalleghem GC, Fane ME, Daignault SM, Matigian N, Scott EK, Smith AG, Stehbins SJ, Schaidler H, Weninger W, Gabrielli B, Haass NK (2020) Functional melanoma cell heterogeneity is regulated by MITF-dependent cell-matrix interactions. <https://doi.org/10.1101/2020.06.09.141747>
- Stehn JR, Haass NK, Bonello T, Desouza M, Kottyan G, Treutlein H, Zeng J, Nascimento PRBB, Sequeira VB, Butler TL, Allanson M, Fath T, Hill TA, McCluskey A, Schevzov G, Palmer SJ, Hardeman EC, Winlaw D, Reeve VE, Dixon I, Weninger W, Cripe TP, Gunning PW (2013) A novel class of anticancer compounds targets the actin cytoskeleton in tumor cells. *Clin Cancer Res* 73:5169–5182. <https://doi.org/10.1158/0008-5472.CAN-12-4501>
- Sutherland RM, McCredie JA, Inch WR (1971) Growth of multicell spheroids in tissue culture as a model of nodular carcinomas. *J Natl Cancer Inst* 46:113–120. <https://doi.org/10.1093/jnci/46.1.113>
- Vittadello ST, McCue SW, Gunasingh G, Haass NK, Simpson MJ (2018) Mathematical models for cell migration with real-time cell cycle dynamics. *Biophys J* 114:1241–1253. <https://doi.org/10.1016/j.bpj.2017.12.041>
- Vittadello ST, McCue SW, Gunasingh G, Haass NK, Simpson MJ (2019) Mathematical models incorporating a multi-stage cell cycle replicate normally-hidden inherent synchronization in cell proliferation. *J R Soc Interface* 16:20190382. <https://doi.org/10.1098/rsif.2019.0382>
- Vittadello ST, McCue SW, Gunasingh G, Haass NK, Simpson MJ (2020) Examining go-or-grow using fluorescent cell-cycle indicators and cell-cycle-inhibiting drugs. *Biophys J* 118:1243–1247. <https://doi.org/10.1016/j.bpj.2020.01.036>
- Ward JP, King JR (1997) Mathematical modelling of avascular-tumour growth. *Math Med Biol* 14:39–69. <https://doi.org/10.1093/imammb/14.1.39>
- Ward JP, King JR (1999) Mathematical modelling of avascular-tumour growth II: modelling growth saturation. *Math Med Biol* 16:171–211. <https://doi.org/10.1093/imammb/14.1.39>

Publisher's Note Springer Nature remains neutral with regard to jurisdictional claims in published maps and institutional affiliations.